Synthetic Aperture Radar

Subjects: Computer Science, Information Systems

Contributor: Sung Wook Paek , Sivagaminathan Balasubramanian , Sangtae Kim , Olivier de Weck

SAR constellations

synthetic aperture radar   satellite constellation   small satellite

1. Introduction

Space-based radar observation has growing potentials for monitoring the global biospheric diversity subject to anthropogenic drivers at geological scales [1]. The performance of radar is less affected by weather and sunlight conditions than that of optical sensors. Satellites with onboard sensors can provide comprehensive coverage of remote areas or vast regions that may be too costly for unmanned aerial vehicles (UAVs) or ground-based platforms, provided that all platforms provide congruent results via calibrations [2][3][4]. Therefore, it was Seasat, the first satellite dedicated to remote sensing of the Earth's oceans, that carried the first synthetic aperture radar (SAR) and other radar instruments operable in space. Despite these advantages, miniaturization of radar-carrying satellites was rather slow compared to satellites carrying optical devices due to the lack of commercial-off-the-shelf (COTS) components as well as challenging design requirements for the satellite platform [5][6].

Representative use cases of space-based radar include altimetry, sounding, scatterometry, and so forth in the studies of land, cryosphere, and oceans. Biospheric monitoring is another useful application because radar has high sensitivity in detecting surface changes in a target area and discriminating mobile targets against a background [7]. This paper will consider mainly SAR because of its three-dimensional mapping capability through interferometry. The heritage of Seasat has influenced many of later SAR missions for decades, as listed in Table 1 [8][9][10][11][12][13]; for instance, Shuttle Image Radar (SIR) missions used spare parts of the previous Seasat mission onboard Space Shuttles to test SAR image applications in land use, geology, hydrology, and forestry [14][15]. European Remote-Sensing Satellite (ERS) could obtain radar data in polar regions thanks to its polar orbit. Two different operational modes were available for SAR of ERS, the imaging mode for high resolution (10m) and the wave mode with 30m resolution for vector measurement of ocean waves. Figure 1 describes the acquisition of imagelets during the wave mode, which may be subdivided into the On-Ground Range Compression (OGRC, 5 km × 5 km) mode and the Onboard Range Compression (OBRC, 5 km × 9.6–12 km) mode [16]. The imaging mode, not shown in Figure 1, is identical to the wave mode except that the entire 100 km wide strip is scanned for high-resolution imagery without any movement profile information. This resolution-swath tradeoff is also shown in Advanced Land Observing Satellite (ALOS) whose ScanSAR mode has a coarse 100m resolution but 250–350 km wide swath. This is 3 to 5 times wider than conventional SAR images and is especially useful for monitoring sea ice and rain forest extent with expansive areas of interest [13].
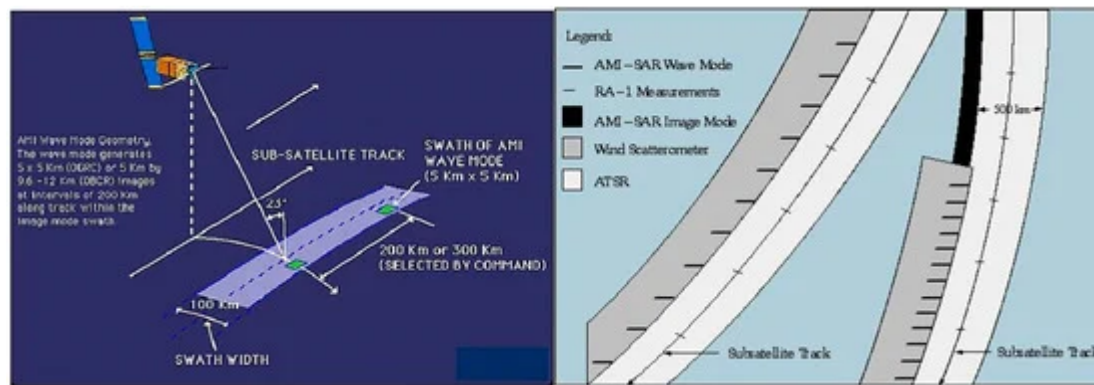
Figure 1. Schematic view of synthetic aperture radar (SAR) onboard European Remote-Sensing Satellite (ERS): (**left**) SAR Wave Mode. (**right**) Switching between SAR Wave mode and SAR Image mode along with their ground swaths. Source: ESA.

Table 1. Synthetic aperture radar missions (2018).

Mission	Country	Duration	Band	Mass (kg)	Swath (km)	Resolution (m, Az-R)
SeaSat	USA	1978	L	2290	100	6–25
SIR-A1/B1	USA	1981, 1984	L	2460	50	7–25/6–13
ERS-1/2	Europe	1991–2010	C	2384	100	6–26
		1995–2011		2516	100	6–26
ALMAZ-1	USSR	1991–1992	S	3420	280	8–15
JERS-1	Japan	1992–1998	L	1400	75	18–18
SIR-C/X	Multi [1]	1994	C,L/X	11,000	90	7.5–13/6–10
RADARSAT-1	Canada	1995–2013	C	3400	500	8–8
SRTM1	Multi [2]	2000	C,X	13,600	100	15–8/8–19
ENVISAT	Europe	2002–2012	C	8210	100	6–9 (SM) [3]
					405	80–8 (SC) [3]
ALOS	Japan	2006–2011	L	3850	70	10–10 (high)
					30	10–30 (polar)
					350	100–100 (SC)
SAR-Lupe	Germany	2006–	X	770 [4]	-	-
RADARSAT-2	Canada	2007–2020	C	2200	18	0.8–1.6 (SL) [5]

Mission	Country	Duration	Band	Mass (kg)	Swath (km)	Resolution (m, Az-R)
					100	8–9 (std)
					500	70–70 (SC)
Cosmo-	Italy	2007–	X	1700	10	1–1 (SL)
SkyMed					40	3–3 (SM)
					200	30–30 (SC)
TerraSAR-X	Germany	2007–2020 [6]	X	1230	10	1–1 (SL)
					30	3–1 (SM)
					270	40–2 (SC)
TecSAR	Israel	2008–	X	260 [4]	-	-
TanDEM-X	Germany	2009–2020 [6]	X	1230	-	Same as TSX
RISAT-1	India	2012–2017	C	1860	10	1–1
					25	3–4
					220	48–8
HJ-1C	China	2012–2016	S	890	100	5–20
KOMPSat-5	S. Korea	2013–2020 [6]	X	1400	18	1–1 (high)
					30	3–3 (std)
					100	5–5 (wide)
Sentinel 1A/B	Europe	2014–	C	2300	80	4–2 (SM)
		2016–			400	43–8 (TS) [7]
ALOS 2	Japan	2014–2020 [6]	L	2120	25	1–3 (SL)
					70	5–9 (SM)
					490	60–45 (SC)
PAZ	Spain	2015–	X	1230	10	1–1 (SL)
					30	3–1 (SM)
					100	20–20 (SC)

Mission	Country	Duration	Band	Mass (kg)	Swath (km)	Resolution (m, Az-R)
RCM	Canada	2017–	C	1430	20	1–1 (SL)
					30	3–10 (SM)
					500	40–40 (SC)
SAOCOM	Argentina	2018–	L	3000	30	10 (Az, SM)
					350	100 (Az, TS)

An important application of SAR is interferometric synthetic aperture radar (InSAR), which was first attempted by time-series analysis of Seasat data. The phase difference in two or more SAR images is measured to yield centimeter- or millimeter-level surface changes over large areas (squares of km) at meter-level resolutions, making InSAR ideal for monitoring surface deformations of Earth [17]. The SAR images capturing the same scene may be acquired at two different times and/or at two slightly different locations. The technique has matured since ERS in the 1990s when the stabilization of satellite orbits allowed for exploiting repeat-ground tracks to visit target areas on a regular basis [18]. Japanese Earth Resources Satellite 1 (JERS-1) also demonstrated two-pass (repeat-pass) cross-track interferometry, meaning that different radar images are obtained from different orbits at different moments [19]. It was the US-Germany joint mission in 2000, called Shuttle Radar Topography Mission (SRTM), which performed single-pass interferometry using one radar antenna onboard a Space Shuttle and another mounted on the end of 60-m mast connected to it [20]. As its name suggests, SRTM was a continuation of the SIR mission in 1994 with a two-antenna configuration. This two-antenna SAR concept is further being developed by German twin-satellite missions as technologies for close-formation flight have become reliable [21]. These missions have new observation modes such as along-track InSAR and SAR polarimetry [22].

Traditional research interests utilizing SAR data focused on geosphere, hydrosphere, and cryosphere among different realms ("-spheres") of Earth science [23][24][25]. Note that the atmosphere is not included in Table 2 because the purpose of radar observation is to minimize the weather influence on its data; ocean wind, for example, is covered by hydrosphere in the context of its surface interactions. Biospheric monitoring herein involves efforts to apply SAR data to agriculture, forestry, and the studies of grasslands and wetlands [26][27]. When it comes to the interactions between the biosphere and the anthroposphere, SAR data could benefit urban management, resource exploration, biomass monitoring, vulnerability studies (e.g., diseases) to name a few [28][29][30][31][32]. The vulnerability studies may also involve interactions between anthroposphere and other realms such as geological events leading to disasters, which again affect biosphere [33]. This trend testifies the newly increasing importance of biospheric monitoring for the already mature field of SAR-based Earth remote sensing.

Table 2. Areas of research utilizing SAR data. Source: German Aerospace Center (DLR) [25].

Category	Application	Temporal Scale			
		Days	**Weeks**	**Months**	**Years**
Biosphere	Deforestation or fire	O	O	O	
	Biodiversity		O	O	O
Cryosphere	Sea ice	O	O		
	Ice cap and glaciers		O	O	
Geosphere	Volcanic activities	O	O		
	Seismic activities	O	O	O	O
	Landslides	O	O		
Hydrosphere	Floods and soil moisture	O	O		
	Ocean currents and tides			O	O

Hitherto, spaceborne SAR instruments have been flown onboard monolithic satellites whose mass is a few tons. On the other side of monolith satellites is the category of small satellites. A small satellite ("Smallsat") weighs less than 500 kg and may be called by other names according to its mass, as listed in Figure 2 [34][35]. Small satellites have become an active area of research as the CubeSat platform was standardized by California Polytechnic State University and Stanford University in 1999 [36]. The CubeSat platform consists of multiple units ("U" s), which is a 10 × 10 × 10 cm cubit volume and is therefore also called "U-class" spacecraft. In terms of mass, a 1 to 3U CubeSat weighs between 1~4 kg, falling into the nanosatellite regime in Figure 2 [37]. Although some of the optical sensors have reached the extent of miniaturization as well as commercialization to fit into a 3U class (e.g., Planet) that has a size of a shoebox, most of the advanced sensors featuring multiple bandwidths require larger volumes, i.e., 6U or more [38][39]. Due to its lower operational frequency (longer wavelength), a radar antenna should be larger than satellite payloads that operate in visible, infrared, or microwave spectrums. The radar system also requires higher power throughputs than optical payloads because they must transmit electromagnetic pulses first to the ground before receiving the backscattered echoes [8][40]. Despite these challenges and constraints, there are several mission plans and startup initiatives for Earth observation missions with SAR-equipped small satellites, which are driven by the aforementioned scientific needs as well as performance-cost advantages of Smallsat constellations [41][42]. Biospheric monitoring is more explicitly manifested as a scientific objective of large SAR satellites, and the same is expected in Smallsat constellations as well [26][43][44].
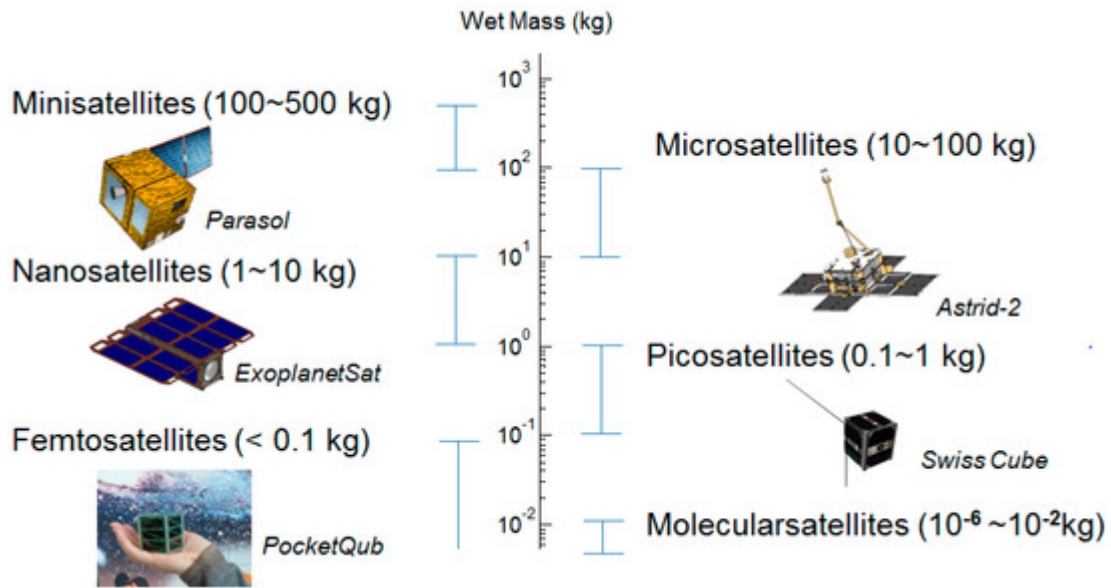
Figure 2. Classification of small satellites. The nanosatellite example shows a 3U CubeSat platform. Source: NASA, National Centre for Space Studies (CNES), Universitat Politècnica de Catalunya, KTH Royal Institute of Technology, École polytechnique fédérale de Lausanne, MIT [34].

2. Synthetic Aperture Radar Satellite Missions

This section surveys spaceborne SAR missions flown already or being planned. First, earlier SAR missions featuring satellite constellations or formation flight are covered in Section 2.1.

2.1. Medium/Large Satellite Constellations

SAR missions in Table 1 have satellite launch mass greater than 500 kg and do not technically fall into the small satellite category. Either medium (500 kg to 1 ton) or large (>1 ton), these satellites were designed following rather conventional principles, less affected by design constraints in mass and volume than small satellites. Nonetheless, deployment and operation details of missions in Table 1 still provide useful guidelines. For example, SAR-Lupe is a 5-satellite system and Cosmo-SkyMed is a 4-satellite system, being the largest and the second-largest (homogeneous) constellations launched so far. Future missions with larger numbers of small satellites would require efficient strategies for constellation design and deployment, for which SAR-Lupe and Cosmo-SkyMed could be good references. TanDEM-X demonstrates various formation flight technologies with two satellites flying close to each other in space, and HJ-1C is an interesting example of a heterogeneous constellation of SAR platforms and optical platforms.

2.1.1. SAR-Lupe

SAR-Lupe is Germany's first military satellite system for global surveillance, delivering radar images for the German Armed Forces for at least ten years since its launch. The spacecraft design by the OHB-System AG utilized a parabolic reflector antenna instead of active beam-steering antennas, which led to major savings in the

cost of instrument development [47][48]. However, the size of a reflector antenna (3.3 m × 2.7 m) poses a major volume constraint during satellite stowage and launch phases as shown in Figure 3, necessitating a dedicated launch for each satellite. The five identical SAR satellites were launched between 2006 and 2008, with individual launches separated by 4 to 8 months [49]. The five satellites are distributed in three orbital planes, marked with plane numbers and corresponding satellites in Figure 3 (right). Orbital planes 1 and 2 are separated by 64° in longitude, and orbital planes 2 and 3 are separated by 65°. Satellite-pairs in orbital planes 1 and 3 have phase angles differing by 69°. Together with a near-polar inclination (98.2°), this satellite arrangement provides the SAR-Lupe constellation with both global coverage and short response time.
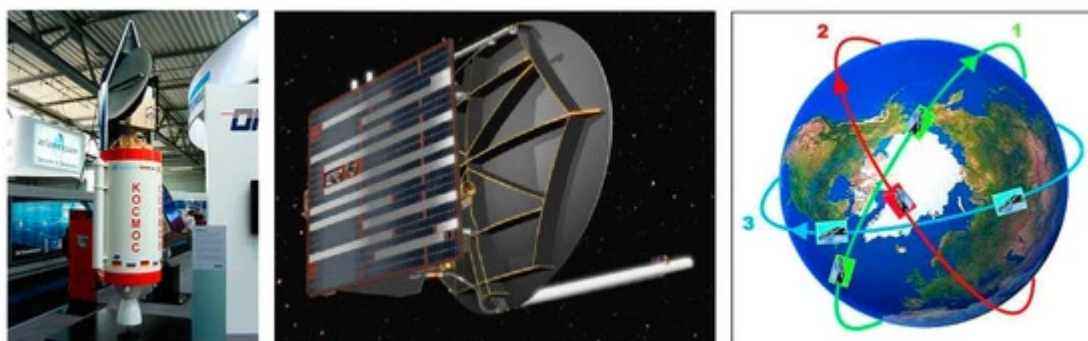

Figure 3. Launch and deployment of SAR-Lupe spacecraft: (**left**) Miniature models of SAR-Lupe and the launch vehicle upper stage. (**middle**) Artist's concept of SAR-Lupe in space. (**right**) Illustration of SAR-Lupe constellation. Source: OHB-System AG.

Observation of SAR-Lupe is made in the X band with a frequency of 9.65 GHz and a wavelength of 3.1 cm, capable of change detection based on SAR interferometry [50]. The stripmap (60 km × 8 km) observation of SAR-Lupe provides nadir-looking scenes, whereas the spotlight (5.5 km × 5.5 km) scenes require the orienting of a spacecraft towards a target area to increase integration time for 0.5 m resolution. When the image acquisition is complete, the spacecraft returns to its standby mode for recharging two 66 Ah lithium-ion batteries with solar panels. Amongst L, S, C, and X bands listed in Figure 4 used for radar sensors, the X band requires the smallest antenna size, which enabled the adoption of a parabolic antenna whose size would be unacceptable in other spectral bands [51]. It also led to a compact design of power systems such as solar arrays providing 550 W at the end of life (EOL), an order of magnitude smaller than the 7 kW power generation (EOL) by ALOS in Table 1. When it comes to onboard batteries, ALOS used nickel-cadmium batteries and SAR-Lupe used lithium-ion for the first time in SAR satellites. Although lithium-ion batteries do not have a "memory effect" suffered by nickel-cadmium batteries, they only became available after more lenient electric-power requirements owing to their higher costs. After all, SAR-Lupe is an interesting example featuring efficient onboard power management at a spacecraft level and a constellation architecture with multiple orbital planes at a higher level, both of which inspired later SAR constellations with small satellites.
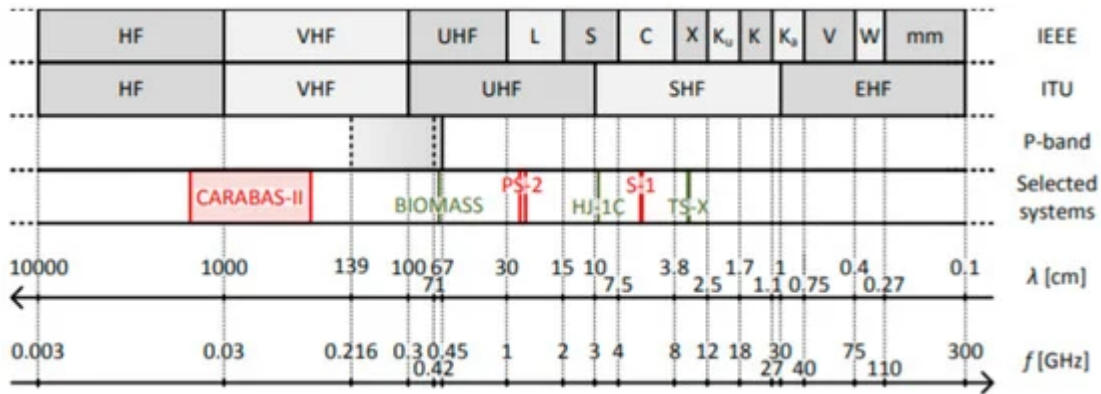
Figure 4. Nomenclature of electromagnetic spectra per the IEEE and International Telecommunication Union (ITU) standards. P-band, which will be used for the European BIOMASS satellite, is defined as the interval 420–450 MHz beyond the L band. As the frequency increases (wavelength decreases) from left to right, the antenna size decreases while the throughput and the susceptibility to rain increases. Source: KTH [51].

2.1.2. Cosmo-SkyMed

COSMO-SkyMed is the acronym for Constellation of Small Satellites for Mediterranean Basin Observation, conceived by the Italian Space Agency. Funded by the Italian Ministry of Research and the Italian Ministry of Defense, the satellite system has dual-use (civilian and military) applications ranging from reconnaissance and risk management to the monitoring of biospheres such as marine/coastal environments, agriculture, and forestry. Because the launch dates of the first satellite (June 2007) and the last satellite (November 2010) are more than three years apart, the constellation size grew rather gradually, operating with intermediate configurations. In each phase, all satellites are in the same orbital plane; the inter-satellite angle decreased from 180° in two-satellite configuration to 90° in a four-satellite configuration in Figure 5. The coverage performance during each stage is listed in Table 3 and Table 4; the mean revisit time of 3 to 6 h at the full-blown state is still longer than three-plane SAR-Lupe whose revisit time is expected to be about an hour [52][53].
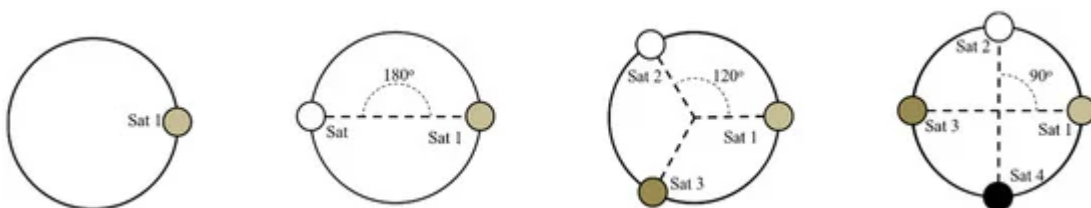

Figure 6. Deployment steps of the COSMO-SkyMed (Constellation of Small Satellites for Mediterranean Basin Observation) configuration.

Table 3. Revisit time of Cosmo-SkyMed during constellation deployment.

Configuration	Average Revisit Time, h		Worst Revisit Time, h	
# Satellites	Left and Right	Right	Left and Right	Right
1	18 to 35 [1] (12 to 23) [2]	37 to 64 (25 to 44)	156 (60)	252 (120)
2	9 to 18 (6 to 12)	19 to 35 (13 to 24)	60 (36)	108 (60)
3	6 to 12 (4 to 8)	13 to 24 (9 to 16)	36 (36)	60 (36)
4	5 to 9 (3 to 6)	10 to 18 (6 to 12)	24 (12)	60 (24)

Table 4. Areal coverage response of Cosmo-SkyMed during constellation deployment.

Configuration	Coverage After 12 h, %		Coverage After 24 h, %	
# Satellites	Left and Right	Right	Left and Right	Right
1	-	-	67 (85)	38 (55)
2	62 [1] (84) [2]	41 (62)	81 (92)	64 (84)
3	88 (98)	62 (84)	96 (99.97)	84 (98)
4	97 (100)	80 (99)	100 (100)	95 (100)

However, the all-in-one-plane architecture of COSMO-SkyMed enables easy transition of its orbital configuration from the nominal mode to several interferometric modes, namely "tandem" and "tandem-like (one-day interferometry)" [54]. First, in tandem interferometry, two satellites are separated in two orbit planes slightly differing in the ascending nodes by 0.08°, denoted as AN (blue) in Figure 5, to guarantee exactly overlapping ground tracks. If the satellites are in a single orbit, they will have slightly different ground tracks due to orbital regression, which is called J2 (Earth's oblateness) effects [55]. The phasing of the two satellites is also adjusted such that the resulting leader-follower pair achieves identical incidence angles. In other words, the two satellites acquire imagery of the same scenes with the same geometry, with a delay of 20 s. Second, in the tandem-like configuration, two satellites stay on the same orbit plane at a distance of 67.5°. This specific angle is used instead of 90° for the tandem-like configuration to achieve "one-day interferometry" with 237/16 repeat cycles; a satellite in this orbit completes 14 and 13/16 revolutions after 16 days (denominator), and the remaining 3/16 revolution to complete an integer number corresponds to 67.5° (=3/16 × 360). The two satellites with this phase spacing visit the same ground target with an exact 1-day interval, as illustrated by COSMO-2 and COSMO-3 in Figure 6 (right). The orbit is a sun-synchronous orbit with an inclination of 97.86°, a nominal altitude of 620 km, and the local time of the ascending node (LTAN) at 6:00 (dawn/dust orbit).
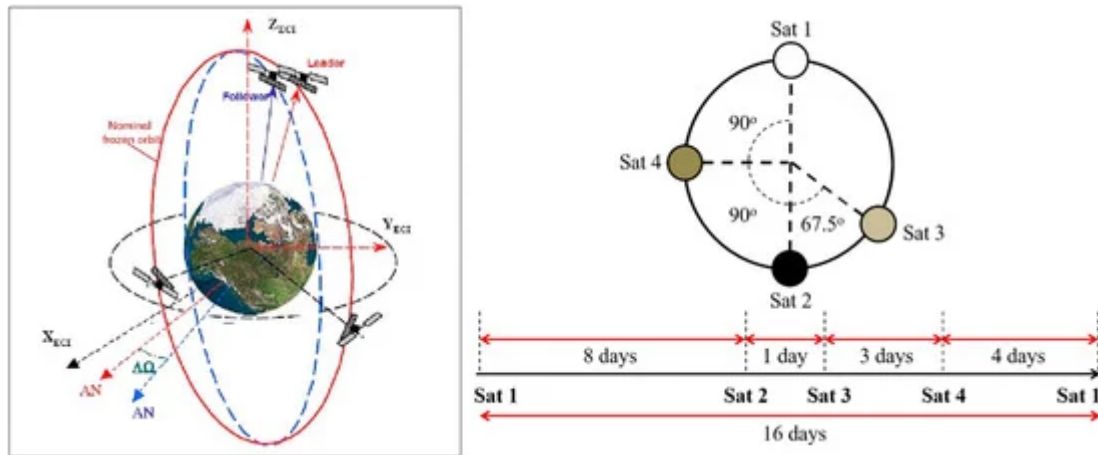
Figure 6. Orbital configuration of the COSMO-SkyMed constellation: (**left**) Tandem configuration. (**right**) Tandem-like configuration. Source: ASI.

The radar transmitter and receiver of each COSMO satellite operate through an electrically steerable multi-beam [56]. This active sensing scheme necessitates a COSMO satellite to manage and store its electrical power more efficiently than other passive SAR systems (e.g., SAR-Lupe). The nominal capacity of a COSMO satellite is 336 Ah, nearly three times larger than that of a SAR-Lupe satellite. The battery cells constituting a COSMO satellite are much smaller in size, however, with 18-mm-wide, 650-mm-long cylindrical footprint depicted in Figure 7 (left). A total of 2016 lithium-ion cylindrical cells are connected in a 9s224p configuration, meaning that 9 cells are first connected in series and then 224 such series-strings, distributed across eight modules in Figure 7 (right), are connected in parallel [57][58]. This configuration provides a maximum current of 650 A (460 A for the 10-s maximum duration) in Spotlight mode and 450 A (330 A for the 10-min maximum duration) in Stripmap mode. The power consumption of a SAR payload in the two modes is 13 kW and 7 kW, respectively. The power subsystem supports a fully polarimetric SAR (PolSAR) where only one linear polarization is received at each interrogation [59].

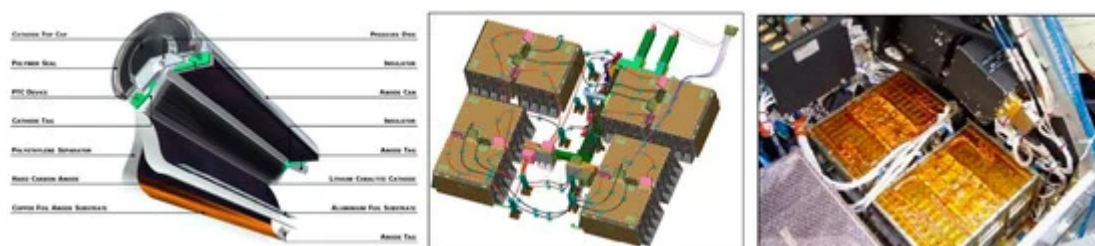**Figure 7.** Energy storage of a COSMO satellite: (**left**) Internal structure of a US18650 hard-carbon lithium-ion cell. (**middle**) Battery packs (8) consisting of 2016 identical batteries. (**right**) SAR-Lupe's 66 Ah battery packs. Source: SONY, ABSL, COM DEV Ltd. [57].

Both SAR-Lupe and COSMO-SkyMed constellations reserve the capability of their satellites to reconfigure their orbits. The resulting launch mass or each satellite was a ton or more, however, electric propulsion seems to be an alternative of chemical propulsion for small satellites to achieve miniaturization, as will be discussed later. Still, medium-to-large satellites will continue to provide responsive access to observation targets, complementing small-

satellite constellations' wide coverage [52][53]. The COSMO-SkyMed mission demonstrated another way of cost reduction using commercial cylindrical lithium-ion batteries for power storage, which can be applied to small satellites as well.

2.1.3. TanDEM-X

The TanDEM-X (TDX, 2007) mission is an extension of the TerraSAR-X (TSX, 2010) mission flying two identical satellites in a close formation to achieve a highly flexible SAR constellation. Following the previous mission name (TerraSAR-X), TanDEM-X means "TerraSAR-X add-on for Digital Elevation Measurement," both of which were implemented through a Public-Private-Partnership of the German Aerospace center (DLR) and European Aeronautic Defense and Space (EADS) Company Astrium (now Airbus Defense and Space). The SAR payload of both TDX and TSX has flight heritage dating back to Shuttle missions such as SIR-X and SRTM, which tested the single-pass SAR interferometry (InSAR) in the X band [60]. The primary objective of the mission is digital elevation model (DEM) generation, for which bistatic processing is employed [61]; both spacecraft, less than 2 km apart as represented in Figure 8 (left), orient their SAR instruments to a common target, which provides different viewing angles [62]. Both spacecraft simultaneously receive echoes of signals transmitted by one of them, which minimizes temporal decorrelation. The resultant single-pass interferometry does not suffer accuracy loss, which would affect repeat-pass (multi-pass) interferometry with a single satellite. An example of bistatic InSAR is the TanDEM-X Forest/Non-Forest Map in which the global raw data set with 50 m × 50 m ground independent pixels were used to classify forest and non-forest areas (urban settlements or freshwater), as shown in Figure 9 [63]. The second interferometric mode is the pursuit monostatic mode, whose Tx/Rx operations are decoupled in two satellites as shown in Figure 8 (right). The amount of temporal decorrelation therein is still small compared to the repeat-pass counterpart. In addition to the aforementioned multistatic (bistatic or monostatic) baseline, the TDX mission concept demonstrated the along-track interferometry (ATI) with four inter- or intra-satellite phase centers. The ATI technique can be used to resolve the velocity of ocean currents, ice drift, and other on-ground objects (e.g., transportation traffic) [64][65][66].
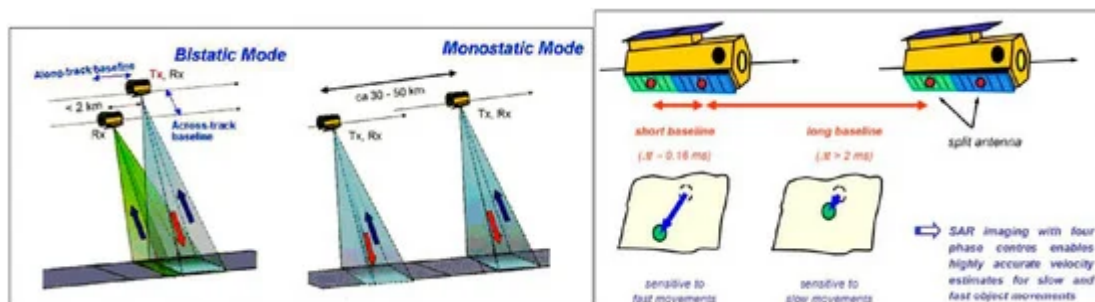

Figure 8. Twin-satellite measurement modes of the TanDEM-X/TerraSAR-X mission: (**left**) Multistatic SAR in a bistatic or monostatic mode for digital elevation measurement. (**right**) Along-track interferometry for object movement detection. Source: DLR.
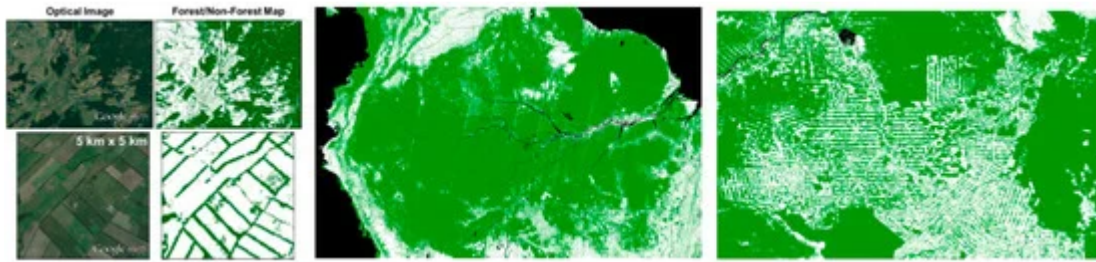
Figure 9. Examples of TanDEM-X Forest/Non-Forest map: (**left**) Germany. (**middle**) South America over Amazon Rainforest. (**right**) Amazon Rainforest, State of Rondonia, Brazil (zoomed-in). Source: DLR.

The TSX spacecraft retains its sun-synchronous dawn-dusk orbit (LTAN = 18:00) with a 515 km altitude and a revisit period of 11 days with 167 orbits, or 15 and 2/11 revolutions per day. The TDX orbit uses eccentricity-inclination separation with respect to the TSX orbit, through which the two spacecraft leave a helix-shaped trajectory relative to a virtual reference in between. The procedures for eccentricity-inclination separation and the relative trajectory are depicted in Figure 10. First, the ascending node of the TDX orbit plane is shifted by a small offset angle to provide horizontal distancing with maximum distance at equator crossings, and the subsequent eccentricity offset provides vertical (radial) distancing maximized at the poles. Small changes in the argument of perigee may also be made to increase inter-satellite distance in medium latitude regions. This kind of orbit and its building procedure have been proposed for consistent separation distance, which in turn reduces collision hazards evenly along the orbit [67][68].
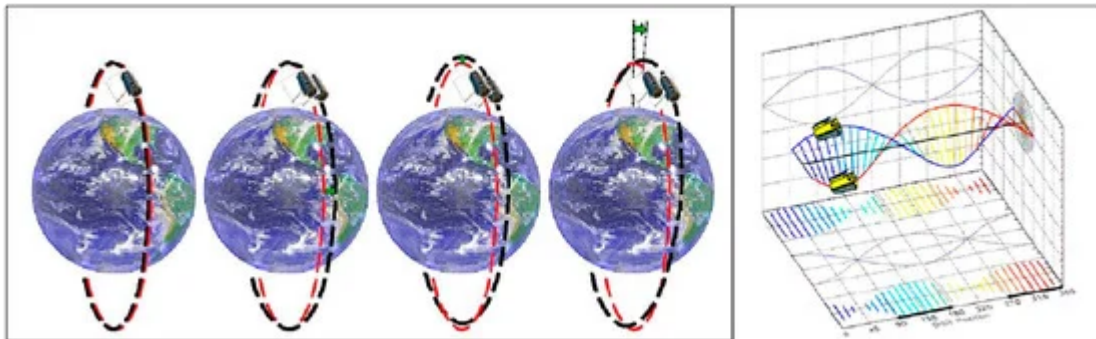

Figure 10. Illustration of TDX-TSX flight formation: (**left**) Formation-building procedures (from left to right): identical orbits, horizontal plane rotation, eccentricity offset, and perigee rotation. (**right**) Helix trajectory in the relative coordinates (numbered axis: angular position in orbit, unnumbered axes: along-track and cross-track position). Source: DLR.

The remote sensing data obtained from TSX/TDX missions have been widely shared with and studied by the scientific community including the TanDEM-X Forest/Non-Forest Map available free of charge online [25][69]. Differencing digital elevation models taken at different moments in time can be applied to monitor climate change, for example, in polar regions. For the first time, pan-Arctic InSAR is made possible with TDX and was applied to observations of a thaw slump in the Mackenzie River Delta, Canada whose aerial photo is provided in Figure 11A [70][71]. The swamp whose DEM was taken in 2015, shown in Figure 11B, has grown in size compared to 2011,

which is represented by negative height changes (depression) in Figure 11C. In addition to this differential InSAR (DInSAR), polarimetric InSAR (Pol-InSAR) by TSX/TDX enables multi-temporal, detailed vertical mapping of croplands and wetlands [72][73][74]. Lastly, 3D SAR images can be constructed from multitudes of 2D SAR images taken at slightly different angles, which reduces ambiguity in pixels with the identical range from satellite but different terrain elevations. This technique of SAR tomography is being applied to deformation analysis of rigid bodies including glaciers and urban infrastructure, as shown in Figure 12 [70][75].

Figure 11. Mackenzie River Delta, Canada: (**A**) Aerial snapshot of a thaw slump. (**B**) Sentinel-2 L1C. Image containing the slump in August 2017. (**C**) Digital elevation model (DEM) processing results after single-pass TanDEM-X observation in June 2015. Source: ETH Zurich.
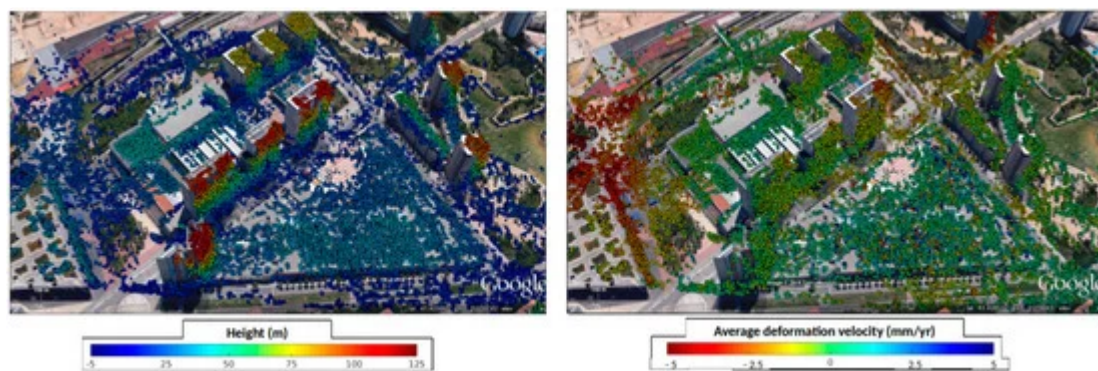

Figure 12. 3D point cloud representing parameters estimated from SAR tomographic inversion on a. Stack of 50 TerraSAR-X images over Barcelona, Spain: (**left**) Ground height. (**right**) Average deformation rate. Source: ETH Zurich.

The nominal design life of TSX and TDX spacecraft has ended in 2012 and 2015, but as of March 2016, the two spacecraft were still operational with similar amounts of residual propellant (TSX: 55%, TDX: 56%) [76]. The fact that calibration of radar instruments did not show any signs of degradation implies the future possibility of extending the lifetime of a medium-sized SAR spacecraft if desired; on-orbit servicing was first demonstrated to refuel a communications satellite in 2020 [77]. The residual capacity of onboard lithium-ion batteries is a function of time, gauging 74% and 82% of the initial 108 Ah for TSX and TDX, respectively. The available spacecraft power has decreased from the peak power of 1.8 kW at the beginning of life (BOL) to the orbital average of 800 watts at the end of life (EOL), which could affect the capability of radar radiation and data communications. The design life of smaller SAR satellites is significantly shorter (<3 years) where the degraded performance should be taken into account for constellation deployment and maintenance because refueling them would not be economical [52][78].

2.2. Small Satellite Constellations

Sub-100 kg microsatellites are currently the lightest small-satellite class in which SAR has been implemented. Many of these SAR satellites are being developed by start-up companies for commercial purposes and feature rapid design iterations between generations. batteries for power storage, which can be applied to small satellites as well.

2.2.1. ICEYE-X1/X2 (85 kg)

Developed by ICEYE in Finland and launched in 2018, ICEYE-X1 is known as the first SAR in microsatellite class with a design mass of 70 kg as well as the country's first commercial satellite [79]. In its launch configuration, ICEYE-X1 has a size of 0.7 m (H) × 0.6 m (W) × 0.4 m (D); its X-band antenna has a length of 3.25 m when deployed [80][81]. With 2 to 3 years of designed life, ICEYE-X1 has a similar shape as the Micro XSAR proto-flight model or the SmallSat InSAR concept. Compared to this proof-of-concept version, ICEYE-X2 features increased form factors (0.8 m x 0.8 m x 0.6 m before deployment, 85 kg) to improve the SAR performance, as shown in Figure 13. The RF peak power of ICEYE-X2 is 4 kW, more than twice the ICEYE-X1 capacity, and its SAR imagery resolution also improved from 10 m to a sub-meter level [82]. The fast design iteration can be seen from the launch dates of the two satellites, January 2018 and December 2018, separated by less than a year. The follow-on satellites, ICEYE-X4 and ICEYE-X5, have identical design specifications as ICEYE-X2 and have been launched together in July 2019, which is probably the first case of launching multiple SAR satellites simultaneously. The ICEYE-X3, also called Harbinger, is a military-purpose variant featuring field-effect electric propulsion and high-rate laser communications capabilities whose payload operations demand 3 kW peak power. Harbinger is no longer classified as a microsatellite because its launch mass is 150 kg falling into the minisatellite class. All ICEYE spacecraft except X3 use Sun-synchronous orbits with inclination values of 97.56° or 97.77°; ICEYE-X3 instead uses an inclined orbit with 40.0° for increased visit frequencies in mid- to low-latitude regions [83]. The fully-blown constellation, with a total of 18 ICEYE satellites launched by 2021, will provide an average of 3-h revisit interval around the globe to observe sea ice movements, marine oil spills, and illegal fishing vessels. In addition to its fast design iteration, the fact that ICEYE is the first Finnish commercial satellite exemplifies a strategy of jumpstarting the SAR satellite development, instead of optical/infrared observation satellites, for Earth remote sensing and its data commercialization.

Figure 13. ICEYE series: (**left**) ICEYE-X1. (**middle**) ICEYE-X2, X4, X5. (**right**) ICEYE-X3 (Harbinger). Source: ICEYE, York Space Systems.

2.2.2. MicroSAR (65 kg)

The MicroSAR system is a proposal by Kongsberg Satellite Services and Space Norway, tailored for maritime monitoring. It is equipped with a C-band 800 W radar transmitter and an onboard automatic identification system (AIS) for vessel tracking [84]. The launch mass of MicroSAR is 65 kg including a 3.8 m x 1.8 deployable reflector illustrated in Figure 14 (left). Figure 14 (right) provides a pictorial description of expected revisit times achieved by eight satellites in two orbit planes in the arctic region. Low-latency tasking and data delivery are possible via a network of twenty ground stations adapted for small satellites across continents and oceans including the Arctic Circle (Svalbard) and Antarctica (Troll Station). Although any MicroSAR satellite has not been launched yet, it represents an example of prioritizing the ground station infrastructures, which have been jointly utilized by Cosmo-SkyMed and NovaSAR so far. As the demands for SAR data increase and small satellites play a bigger role therein, its market will be segmented into launch services (e.g., Electron rocket), ground stations (e.g., KSAT), data analytics, and so forth dedicated to small satellites and/or spaceborne SAR.
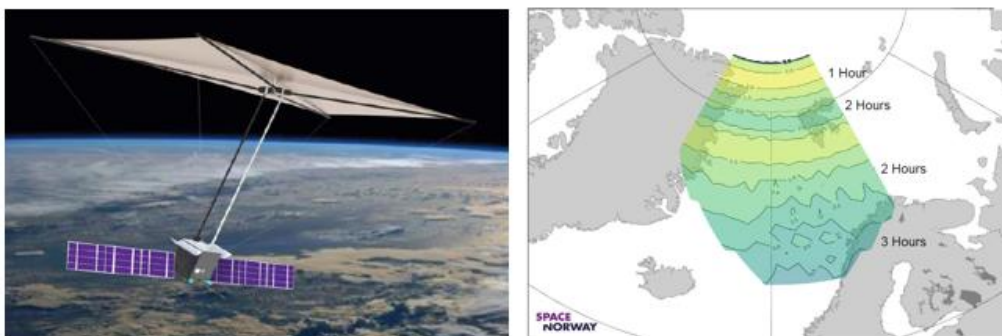

Figure 14. MicroSAR: (left) Artist's rendition. (right) Simulated revisit times in the Norwegian Sea and the Greenland Sea. Source: Kongsberg Satellite Services.

2.2.3. Capella X-SAR (48 kg)

This SAR constellation, developed by Capella Space, will have 36 satellites by 2023, 6 of which are already in orbit [85]. The first satellite, Capella 1 or Denali, has a launch mass of less than 50 kg with an origami-like antenna shown in Figure 15 (left). The second satellite, Capella 2 or Sequoia, is about twice as large as the predecessor, accommodates a 600 W transmitter and a mesh-based $8m^2$ reflector that is shown in Figure 15 (right) to achieve sub-meter ground resolution [86]. Following the launch of Capella 1 in December 2018 and Capella 2 in March 2020, three satellites (Capella 3, 4, 5) will be launched with further design improvements, constituting a "Whitney" sub-constellation. Another satellite called Capella X was launched into an inclined orbit with 45° inclination in May 2020. The Whitney sub-constellation and others will constitute the "Capella 36" constellation, and the coverage performance of possible configurations in between is summarized in Table 5. Capella Space is using the satellite ground station service provided by Amazon Web Services (AWS) for the rapid delivery of satellite data to its customers [87].

Figure 15. Capella series: (**left**) Capella 1 (Denali). (**right**) Capella 2 (Sequoia). Source: Capella Space.

Table 5. Capella X-SAR observation modes and revisit performance.

Total # Satellite	6	12	24	36
# orbit planes	2	4	8	12
Average revisit (h)	<4	<2	1	<1
Maximum revisit (h)	12	6	4	<2
InSAR revisit (h)	24	12	6	4

2.2.4. Umbra-SAR (50 kg)

Umbra Lab, a US startup is developing the Umbra-SAR constellation whose first satellite, named Umbra-SAR 2001, will be launched in 2020 [88]. Each Umbra- is a 50 kg satellite equipped with an X-band SAR, twelve of which will constitute the Umbra-SAR constellation [89]. The proposed SAR targets include subsidence/sinking due to water pumping or oil drilling, underground tunnels near borders, supply chain monitoring, precision farming, and maritime compliance [90]. The software-defined radar of Umbra-SAR 2001, a SAR analog of software-defined radio (SDR), is the first of its kind and is expected to provide the possibility of multipurpose radar implementation with hardware re-use [91].
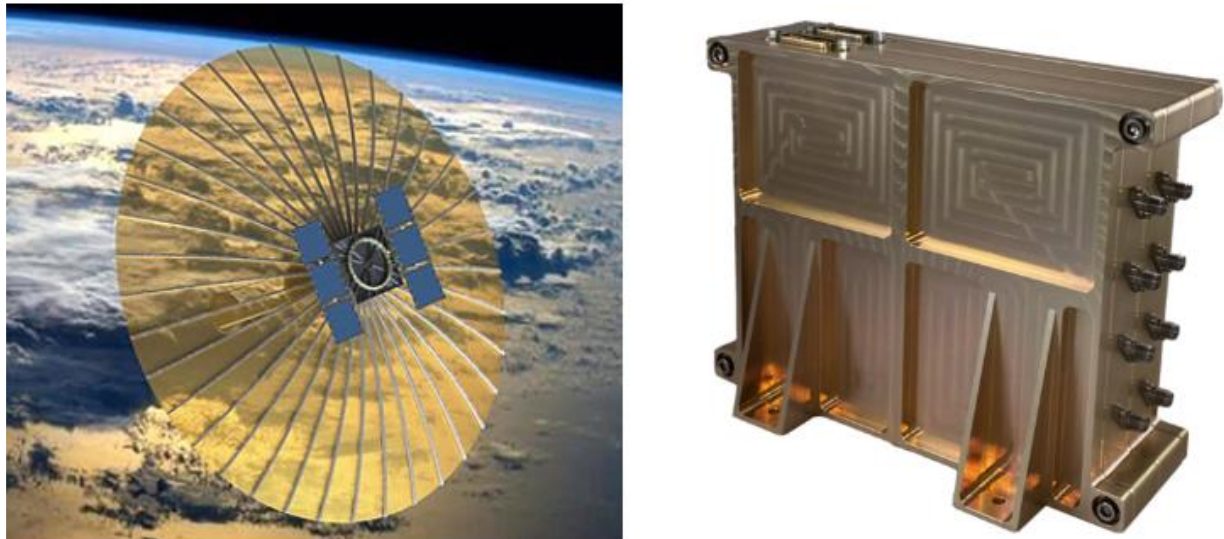
Figure 16. Umbra-SAR 2001: (**left**) Deployable antenna. (**right**) software-defined radar. Source: Umbra Lab, Starbridge.

3. Summary and Conclusion

In Earth remote sensing, it is often useful to understand the data generation flows from the very beginning, satellites in this case. The SAR instruments onboard the spaceborne platforms, in particular, have been following a relatively simple flight heritage dating back to Seasat and ERS satellites (Section 1). New space missions represented by small satellites, however, are driving cost reduction and changing the design paradigm of space-based SAR platforms (Section 2) and the analytics philosophy of remotely-sensed big data therefrom [92][93][94][95][96]. Table 6 summarizes the power and mass specifications of different SAR missions. The smallest radar cubesat (non-SAR), RaInCube, has a battery capacity of an electric scooter (~10Ah) and small SAR satellites have ratings similar to TECSAR [97].

Table 6. Power and mass of different SAR missions from nanosatellites to medium satellites.

Mission	Battery Capacity	SolarArray Power	Payload PeakPower	Payload Mass	Total Launch Mass
RaInCube	~10 Ah	45 W	22 W	5.5 kg	12 kg
TECSAR	45 Ah	1600 W	850 W	100 kg	260 kg

HJ-1C	80 Ah	1100 W	-	200 kg	890 kg
SAR-Lupe	108 Ah	-	1800 W	394 kg	1230 kg
TSX	132 Ah	-	-	-	770 kg
Cosmo-SkyMed	336 Ah	40,000 W	7000 W	-	1700 kg

Table 7 compares the cost breakdown of select SAR constellations [98]. The design of an Earth-observing constellation requires a balance between its performance and the deployment cost [99][100]. Both the cost per kilogram (1st column) and the satellite cost for each mission (3rd column) include the launch cost, whose proportion is given by percentage (4th column). The cost per satellite is similar between ICEYE and Capella X-SAR, so it can be regarded that the cost of further reducing satellite sizes seems to counterbalance the benefit of lower launch costs due to the reduced mass; in both ICEYE and Capella X-SAR missions, the second generation had a larger volume and mass than the first generation, which implies the limitations of over-downsizing. When it comes to the launch cost, it may be reduced by making use of rideshares, mass deployment, and/or reusable launch vehicles. Albeit its higher degree of freedom in launch options, small rockets are not economically competitive at the moment; Electron costs 5 million USD (MUSD) to launch a 150–225 kg payload to a 500 km Sun-synchronous orbit whilst SpaceX's rideshare program takes 1 MUSD under similar conditions [101][102]. The operational cost may also be reduced by sharing the established ground station network such as KSAT or Amazon Web Service (AWS), the latter of which has open-price policies throughout the globe in the range of 10–20 USD per minute [103]. After all, cost reduction, which has motivated the transition from large SAR satellites to small ones, will continue to happen in multiple cost components. Last but not least, constellation management and budgeting should consider operational uncertainties and risks in space environments owing to the solar activities or the mega-constellations of space-internet satellites [104].

Table 7. Cost breakdown of small-satellite SAR missions.

Mission	Cost/kg (kUSD)	Sat Mass (kg)	SatCost (MUSD)	Launch Cost (%)	Launch Vehicle	Ground Station
ICEYE	82	85	7	42	Falcon 9, Electron	KSAT
SAR-Lupe	117	770	90	24	Kosmos	DLR

TSX/TDX	143	1230	117	20	Dnepr	DLR
NovaSAR	146	400	59	23	PSLV	KSAT
Capella X-SAR	163	48	8	21	Falcon 9, PSLV, Electron	AWS
Cosmo-SkyMed	214	1700	364	13	Soyuz	KSAT

References

1. Crutzen, P.J. The "anthropocene". J. Phys. IV (Proc.) 2002, 12, 1–5.

2. Bae, S.; Levick, S.R.; Heidrich, L.; Magdon, P.; Leutner, B.F.; Wöllauer, S.; Serebryanyk, A.; Nauss, T.; Krzystek, P.; Gossner, M.M.; et al. Radar vision in the mapping of forest biodiversity from space. Nat. Commun. 2019, 10, 4757.

3. Kato, A.; Wakabayashi, H.; Hayakawa, Y.; Bradford, M.; Watanabe, M.; Yamaguchi, Y. Tropical forest disaster monitoring with multi-scale sensors from terrestrial laser, UAV, to satellite radar. In Proceedings of the 2017 IEEE International Geoscience and Remote Sensing Symposium (IGARSS), Fort Worth, TX, USA, 23–28 July 2017; pp. 2883–2886.

4. Matese, A.; Toscano, P.; Di Gennaro, S.F.; Genesio, L.; Vaccari, F.P.; Primicerio, J.; Belli, C.; Zaldei, A.; Bianconi, R.; Gioli, B. Intercomparison of UAV, aircraft and satellite remote sensing platforms for precision viticulture. Remote Sens. 2015, 7, 2971–2990.

5. Peral, E.; Im, E.; Wye, L.; Lee, S.; Tanelli, S.; Rahmat-Samii, Y.; Horst, S.; Hoffman, J.; Yun, S.-H.; Imken, T.; et al. Radar technologies for earth remote sensing from cubesat platforms. Proc. IEEE 2018, 106, 404–418.

6. Marinan, A.D.; Hein, A.G.A.G.I.; Lee, Z.T.; Carlton, A.K.; Cahoy, K.; Milstein, A.B.; Shields, M.W.; DiLiberto, M.T.; Blackwell, W.J. Analysis of the Microsized Microwave Atmospheric Satellite (MicroMAS) Communications Anomaly. J. Small Satell. 2018, 7, 683–699.

7. Space Advisory Company. Potential Synthetic Aperture Radar Applications of Small Satellites. 2017. Available online: http://www.unoosa.org/documents/pdf/psa/activities/2017/SouthAfrica/slides/ Presentation23.pdf (accessed on 18 April 2020).

8. Moreira, A.; Prats-Iraola, P.; Younis, M.; Krieger, G.; Hajnsek, I.; Papathanassiou, K.P. A tutorial on synthetic aperture radar. IEEE Geosci. Remote Sens. Mag. 2013, 1, 6–43.

9. Lubin, D.; Massom, R. Polar Remote Sensing: Volume I: Atmosphere and Oceans; Springer Science & Business Media: Berlin/Heidelberg, Germany, 2006; p. 389.

10. PCI Geomatics. KOMPSAT-5. 2015. Available online: https://www.pcigeomatics.com/geomatica-help/references/gdb_r/KOMPSAT5.html (accessed on 26 July 2020).

11. ESA eoPortal, SIR-A (Shuttle Imaging Radar)/OSTA-1 Payload on STS-2 Mission. 2020. Available online: https://directory.eoportal.org/web/eoportal/satellite-missions/s/sir-a (accessed on 26 May 2020).

12. ESA. ERS Overview. 2020. Available online: https://www.esa.int/Applications/Observing_the_ Earth/ERS_overview (accessed on 26 May 2020).

13. Alaska Satellite Facility. ALOS Phased Array type L-band Synthetic Aperture Radar. 2020. Available online: https://asf.alaska.edu/data-sets/sar-data-sets/alos-palsar/alos-palsar-about/ (accessed on 23 June 2020)

14. Moore, J.W. OSTA-1: The Space Shuttle's first scientific payload. In Proceedings of the 33rd IAF/IAC Congress, Paris, France, 27 September–October 2 1982.

15. Elachi, C.; Brown, W.E.; Cimino, J.B.; Dixon, T.; Evans, D.L.; Ford, J.P.; Saunders, R.S.; Breed, C.; Masursky, H.; McCauley, J.F.; et al. Shuttle Imaging Radar Experiment. Science 1982, 218, 996–1003.

16. Attema, E.P.W. The Active Microwave Instrument On-Board the ERS-1 Satellite. Proc. IEEE 1991, 79, 791–799.

17. Klees, R.; Massonnet, D. Deformation measurements using SAR interferometry: Potential and limitations. Geologie en Mijnbouw 1998, 77, 161–176.

18. Baghdadi, N.; Zribi, M. Microwave Remote Sensing of Land Surfaces: Techniques and Methods; Elsevier: Amsterdam, The Netherlands, 2016; p. 68.

19. Pepe, A.; Calò, F. A review of interferometric synthetic aperture RADAR (InSAR) multi-track approaches for the retrieval of Earth's surface displacements. Appl. Sci. 2017, 7, 1264.

20. Knight, P.G. (Ed.) Glacier Science and Environmental Change; John Wiley & Sons: Hoboken, NJ, USA, 2008.

21. Rizzoli, P.; Martone, M.; Gonzalez, C.; Wecklich, C.; Tridon, D.B.; Bräutigam, B.; Markus, B.; Schulze, D.; Fritz, T.; Huber, M.; et al. Generation and performance assessment of the global TanDEM-X digital elevation model. ISPRS J. Photogramm. 2017, 132, 119–139.

22. Romeiser, R.; Johannessen, J.; Chapron, B.; Collard, F.; Kudryavtsev, V.; Runge, H.; Suchandt, S. Direct Surface Current Field Imaging from Space by along-Track InSAR and Conventional SAR. In Oceanography from Space; Barale, V., Gower, J., Alberotanza, L., Eds.; Springer: Dordrecht, The Netherlands, 2010.

23. Roth, A.; Marschalk, U.; Winkler, K.; Schättler, B.; Huber, M.; Georg, I.; Künzer, C.; Dech, S. Ten years of experience with scientific TerraSAR-X data utilization. Remote Sens. 2018, 10, 1170.

24. Young, N. Applications of Interferometric Synthetic Aperture Radar (InSAR): A small research investigation. 2018. Available online: https://www.researchgate.net/publication/328773243_Applications_ of_Interferometric_Synthetic_Aperture_Radar_InSAR_a_small_research_investigation (accessed on 23 June 2020)

25. DLR Microwaves and Radar Institute. Research results and projects (2011–2017). 2017. Available online: https://www.dlr.de/hr/Portaldata/32/Resources/dokumente/broschueren/HR-Institute-Status-Report-2011-2017.pdf (accessed on 3 June 2020).

26. Chu, T.; Guo, X. Remote sensing techniques in monitoring post-fire effects and patterns of forest recovery in boreal forest regions: A review. Remote Sens. 2014, 6, 470–520.

27. White, L.; Brisco, B.; Dabboor, M.; Schmitt, A.; Pratt, A. A collection of SAR methodologies for monitoring wetlands. Remote Sens. 2015, 7, 7615–7645.

28. Xiong, S.; Muller, J.P.; Li, G. The application of ALOS/PALSAR InSAR to measure subsurface penetration depths in deserts. Remote Sens. 2017, 9, 638.

29. Carreiras, J.M.; Quegan, S.; Le Toan, T.; Minh, D.H.T.; Saatchi, S.S.; Carvalhais, N.; Reichstein, M.; Scipal, K. Coverage of high biomass forests by the ESA BIOMASS mission under defense restrictions. Remote Sens. Environ. 2017, 196, 154–162.

30. Adimi, F.; Soebiyanto, R.P.; Safi, N.; Kiang, R. Towards malaria risk prediction in Afghanistan using remote sensing. Malar. J. 2010, 9, 125.

31. Bøgh, C.; Lindsay, S.W.; Clarke, S.E.; Dean, A.; Jawara, M.; Pinder, M.; Thomas, C.J. High spatial resolution mapping of malaria transmission risk in the Gambia, west Africa, using LANDSAT TM satellite imagery. Am. J. Trop. Med. Hyg. 2007, 76, 875–881.

32. Rogers, D.J.; Randolph, S.E.; Snow, R.W.; Hay, S.I. Satellite imagery in the study and forecast of malaria. Nature 2002, 415, 710–715.

33. Braun, A. Radar Satellite Imagery for Humanitarian Response. Ph.D. Thesis, Universit of Tübingen, Tübingen, Germany, 2019.

34. Paek, S.W. Reconfigurable Satellite Constellations for Geo-spatially Adaptive Earth-Observation Missions. Master's Thesis, Massachusetts Institute of Technology, Cambridge, MA, USA, 2012.

35. Tristancho, J. Implementation of a Femto-Satellite and a Mini-Launcher. Master's Thesis, Universitat Politècnica de Catalunya, Barcelona, Spain, 2012.

36. Helvajian, H.; Janson, S.W. Eds. Small Satellites: Past, Present, and Future; Aerospace Press: El Segundo, CA, USA, 2008; ISBN 978-1-884989-22-3.

37. Deepak, R.A.; Twiggs, R.J. Thinking out of the box: Space science beyond the CubeSat. J. Small Satell. 2012, 1, 3–7.

38. Camps, A.; Golkar, A.; Gutierrez, A.; de Azua, J.R.; Munoz-Martin, J.F.; Fernandez, L.; Diez, C.; Aguilella, A.; Briatore, S.; Akhtyamov, R.; et al. FSSCAT, the 2017 Copernicus Masters'"ESA Sentinel Small Satellite Challenge" Winner: A Federated Polar and Soil Moisture Tandem Mission Based on 6U Cubesats. In Proceedings of the IGARSS 2018-2018 IEEE International Geoscience and Remote Sensing Symposium, Valencia, Spain, 22–27 July 2018; IEEE, New York City, NY, USA: 2018; pp. 8285–8287.

39. Wright, R.; Nunes, M.; Lucey, P.; Flynn, L.; George, T.; Gunapala, S.; Ting, D.; Rafol, S.; Soibel, A.; Ferrari-Wong, C.; et al. HYTI: Thermal hyperspectral imaging from a CubeSat platform. Proc. SPIE 2019, 11131, 111310G.

40. Saito, H.; Hirokawa, J.; Tomura, T.; Akbar, P.R.; Pyne, B.; Tanaka, K.; Mita, M.; Kaneko, T.; Watanabe, H.L.; Ijichi, K. Development of Compact SAR Systems for Small Satellite. In Proceedings of the IGARSS 2019–2019 IEEE International Geoscience and Remote Sensing Symposium, Yokohama, Japan, 28 July–2 August 2019; IEEE, New York City, NY, USA: 2019; pp. 8440–8443.

41. Filippazzo, G.; Dinand, S. The Potential Impact of Small Satellite Radar Constellations On Traditional Space System. In Proceedings of the 5th Federated and Fractionated Satellite Systems Workshop, Ithaca, NY, USA, 2–3 November 2017.

42. Kim, Y.; Kim, M.; Han, B.; Kim, Y.; Shin, H. Optimum design of an SAR satellite constellation considering the revisit time using a genetic algorithm. Int. J. Aeronaut. Space Sci. 2017, 18, 334–343.

43. NASA. NASA-ISRO SAR (NISAR) Mission Science Users' Handbook. 2019. Available online: https://nisar.jpl.nasa.gov/files/nisar/NISAR_Science_Users_Handbook.pdf (accessed on 3 June 2020)

44. Ocampo-Torres, F.J.; Gutiérrez-Nava, A.; Ponce, O.; Vicente-Vivas, E.; Pacheco, E. On the progress of the nano-satellite SAR based mission TOPMEX-9 and specification of potential

applications advancing the Earth Observation Programme of the Mexican Space Agency. In Proceedings of the Conference on Space Optical Systems and Applications, Santa Monica, CA, USA, 11-13 May 2011; pp. 102–109.

45. Freeman, A. Design principles for smallsat SARs. In Proceedings of the 32nd Annual AIAA/USU Conference on Small Satellites, Logan, UT, USA, 4-9 August 2018.

46. Farquharson, G.; Woods, W.; Stringham, C.; Sankarambadi, N.; Riggi, L. The Capella Synthetic Aperture Radar Constellation. In Proceedings of the EUSAR 2018; 12th European Conference on Synthetic Aperture Radar, Aachen, Germany, 4–7 June 2018; VDE Verlag, Berlin, Germany: 2018; pp. 1–5.

47. Safy, M. Synthetic Aperture Radar for Small Satellite. Int. J. Innov. Technol. Eng. 2019, 9, 3435–3440.

48. Braun, H.M.; Knobloch, P.E. SAR on Small Satellites-Shown on the SAR-Lupe Example. In Proceedings of the International Radar Symposium, 2007 (IRS 2007), Cologne, Germany, 5–7 September 2007.

49. Zemann, J.L.; Nitschko, T.; Supper, L.; Konigsreiter, G. The Deployable Boom Assembly for SAR-Lupe. In Proceedings of the 28th ESA Antenna Workshop, Estec Noordwijk, The Netherlands, 31 May–3 June 2005.

50. Clark, R.M. The Technical Collection of Intelligence; CQ Press, Washington, DC, USA: 2010.

51. Soja, M.J. Modelling and Retrieval of Forest Parameters from Synthetic Aperture Radar Data; Chalmers University of Technology: Gothenburg, Sweden, 2014.

52. Paek, S.W.; de Weck, O.L.; Smith, M.W. Concurrent design optimization of Earth observation satellites and reconfigurable constellations. J. Brit. Interplanet. Soc. 2017, 70, 19–35.

53. Paek, S.W.; Kim, S.; de Weck, O.L. Optimization of reconfigurable satellite constellations using simulated annealing and genetic algorithm. Sensors 2019, 19, 765.

54. Covello, F.; Battazza, F.; Coletta, A.; Lopinto, E.; Fiorentino, C.; Pietranera, L.; Valentni, G.; Zoffoli, S. COSMO-SkyMed an existing opportunity for observing the Earth. J. Geodyn. 2010, 49, 171–180.

55. Paek, S.W.; Kim, S.; Kronig, L.G.; de Weck, O.L. Sun-synchronous repeat ground tracks and other useful orbits for future space missions. Aeronaut. J. 2020, 124, 917–939.

56. Candela, L.; Caltagirone, F. Cosmo-SkyMed: Mission Definition, Main Application and Products. In Proceedings of the ESA POLinSAR Workshop. Frascati, Italy, 14–16 January 2003. ESA Publications Division, Noordwijk, The Netherlands.

57. Csizmar, A.; Richards, L.; Scorzafava, E.; Daprati, G.; Perrone, G. COSMO-SkyMed, First Lithium-Ion Battery for Space-based Radar. In Proceedings of the 7th European Space Power

Conference, Stresa, Italy, 9–13 May 2005.

58. Troutman, J. SONY 18650 Hard Carbon Cell and SONY 18650 Hard Carbon Mandrel Cell. In Proceedings of the NASA Battery Workshop, 2011 NASA Battery Workshop, Huntsville, AL, USA, 15 November 2011.

59. Lombardo, P. A multichannel spaceborne radar for the COSMO-SkyMed satellite constellation. In Proceedings of the 2004 IEEE Aerospace Conference Proceedings (IEEE Cat. No. 04TH8720), Big Sky, MT, USA, 6–13 March 2004; IEEE, New York City , NY, USA: 2004; Volume 1.

60. Ochs, S.; Pitz, W. The terrasar-x and tandem-x satellites. In Proceedings of the 2007 3rd International Conference on Recent Advances in Space Technologies, Istanbul, Turkey, 14–16 June 2007; IEEE, New York City, NY, USA: 2007; pp. 294–298.

61. Krieger, G.; Zink, M.; Bachmann, M.; Bräutigam, B.; Schulze, D.; Martone, M.; Rizzoli, P.; Steinbrecher, U.; Antony, J.W.; De Zan, F.; et al. TanDEM-X: A radar interferometer with two formation-flying satellites. Acta Astronaut. 2013, 89, 83–98.

62. Moreira, A.; Krieger, G.; Hajnsek, I.; Hounam, D.; Werner, M.; Riegger, S.; Settelmeyer, E. TanDEM-X: A TerraSAR-X Add-On Satellite for Single-Pass SAR Interferometry. In Proceedings of IGARSS 2004, Anchorage, AK, USA, 20–24 September 2004.

63. Martone, M.; Rizzoli, P.; Wecklich, C.; Gonzalez, C.; Bueso-Bello, J.-L.; Valdo, P.; Schulze, D.; Zink, M.; Krieger, K.; Moreira, A. The Global Forest/Non-Forest Map from TanDEM-X Interferometric SAR Data. Remote Sens. Environ. 2018, 205, 352–373.

64. Krieger, G.; Fiedler, H.; Moreira, A. Bi-and multistatic SAR: Potentials and challenges. Proc. EUSAR 2004, 34, 365–370.

65. Krieger, G.; Fiedler, H.; Houman, D.; Moreira, A. Analysis of system concepts for bi-and multi-static SAR missions. In Proceedings of the IGARSS 2003. 2003 IEEE International Geoscience and Remote Sensing Symposium. Toulouse, France, 21–25 July 2003; IEEE, New York City, NY, USA: 2003; Volume 2, pp. 770–772.

66. Gill, E.; Runge, H. Tight formation flying for an along-track SAR interferometer. Acta Astronaut. 2004, 55, 473–485.

67. Krieger, G.; Hajnsek, I.; Papathanassiou, K.P.; Younis, M.; Moreira, A. Interferometric synthetic aperture radar (SAR) missions employing formation flying. Proc. IEEE 2010, 98, 816–843.

68. Satellite Configuration for Interferometric and/or Tomographic Remote Sensing by Means of Synthetic Aperture Radar (SAR). U.S. Patent No 6,677,884, 13 January 2004.

69. DLR. Earth Observation Center. 2020. Available online: https://geoservice.dlr.de/web/maps/tdmforest (accessed on 3 June 2020).

70. ETH Zurich. Chair of Earth Observation and Remote Sensing. 2020. Available online: https://eo.ifu.ethz.ch/forschung/Techniques.html#par_textimage_2091550249 (accessed on 3 June 2020).

71. Ullmann, T.; Büdel, C.; Baumhauer, R. Characterization of arctic surface morphology by means of intermediated TanDEM-X digital elevation model data. Z. Geomorphol. 2017, 61, 3–25.

72. Betbeder, J.; Rapinel, S.; Corpetti, T.; Pottier, E.; Corgne, S.; Hubert-Moy, L. Multitemporal classification of TerraSAR-X data for wetland vegetation mapping. J. Appl. Remote Sens. 2014, 8, 083648.

73. Lopez-Sanchez, J.M.; Ballester-Berman, J.D.; Hajnsek, I. First results of rice monitoring practices in Spain by means of time series of TerraSAR-X dual-pol images. IEEE J. Sel. Top. Appl. Earth Obs. Remote Sens. 2010, 4, 412–422.

74. Koppe, W.; Gnyp, M.L.; Hütt, C.; Yao, Y.; Miao, Y.; Chen, X.; Bareth, G. Rice monitoring with multi-temporal and dual-polarimetric TerraSAR-X data. Int. J. Appl. Earth Obs. 2013, 21, 568–576.

75. Tebaldini, S.; Nagler, T.; Rott, H.; Heilig, A. Imaging the internal structure of an alpine glacier via L-band airborne SAR tomography. IEEE Trans. Geosci. Remote Sens. 2016, 54, 7197–7209.

76. Buckreuss, S.; Zink, M. TerraSAR-X and TanDEM-X mission status. In Proceedings of EUSAR 2016: 11th European Conference on Synthetic Aperture Radar, Hamburg, Germany, 6–9 June 2016; VDE Verlag, Berlin, Germany: 2016; pp. 1–6.

77. Howell, E. Two private satellites just docked in space in historic first for orbital servicing. 2020. Available online: https://www.space.com/private-satellites-docking-success-northrop-grumman-mev-1.html (accessed on 24 July 2020).

78. de Weck, O. A Review of Satellite Constellation Reconfiguration and Its Applications. In Proceedings of the 10th International Workshop on Satellite Constellations & Formation Flying, Glasgow, UK, 16-19 July 2019.

79. Tian, W.; Bian, X.; Shao, Y.; Zhang, Z. On the detection of oil spill with China's HJ-1C SAR image. Aquat. Procedia 2015, 3, 144–150.

80. Guo, H.; Fu, W.; Liu, G. Scientific Satellite and Moon-Based Earth Observation for Global Change; Springer Singapore, 2019; p. 423.

81. Observing Systems Capability Analysis and Review Tool. Satellite: HJ-1C. 2020. Available online: https://www.wmo-sat.info/oscar-staging/satellites/view/171 (accessed on 15 June 2020).

82. Bird, R.; Whittaker, P.; Stern, B.; Angli, N.; Cohen, M.; Guida, R. NovaSAR-S: A low cost approach to SAR applications. In Proceedings of the Conference Proceedings of 2013 Asia-Pacific Conference on Synthetic Aperture Radar (APSAR), Tsukuba, Japan, 23–27 September 2013; IEEE, New York City, NY, USA: 2013; pp. 84–87.

83. Iervolino, P.; Guida, R.; Whittaker, P. NovaSAR-S and maritime surveillance. In Proceedings of the 2013 IEEE International Geoscience and Remote Sensing Symposium-IGARSS, Melbourne, VIC, Australia, 21–26 July 2013; IEEE, New York City, NY, USA: 2013; pp. 1282–1285.

84. Davies, P.; Whittaker, P.; Bird, R.; Gomes, L.; Stern, B.; Sweeting, M.; Cohen, M.; Hall, D. NovaSAR–Bringing Radar Capability to the Disaster Monitoring Constellation, In Proceedings of the 26th Annual USU Conference on Small Satellites, Logan, UT, USA, 13-16 August 2012.

85. Natale, A.; Guida, R.; Bird, R.; Whittaker, P.; Cohen, M.; Hall, D. Demonstration and analysis of the applications of S-band SAR. In Proceedings of the 2011 3rd International Asia-Pacific Conference on Synthetic Aperture Radar (APSAR), Seoul, Korea, 26–30 September 2011; IEEE, New York City, NY, USA: 2011; pp. 1–4.

86. Pauwels, V.; Walker, J.; Grimaldi, S.; Wright, A.; Li, Y. 2019. Improving Flood Forecast Skill Using Remote Sensing Data. Available online: https://www.bnhcrc.com.au/sites/default/files/managed/downloads/ improving_flood_forecast_skill_using_remote_sensing_data_annual_report_2018-2019_final.pdf (accessed on 20 July 2020).

87. Surrey Satellite Technology Ltd., SSTL announces NovaSAR-1 data deal with the Philippines. 2019. Available online: https://www.sstl.co.uk/media-hub/latest-news/2019/sstl-announces-novasar-1-data-deal-with-the-philip (accessed on on 20 July 2020).

88. Gunter's Space Page. Ofeq 8, 10 (TECSAR 1, 2/TechSAR 1, 2). 2020. Available online: https://space.skyrocket.de/doc_sdat/techsar-1.htm (accessed on 15 June 2020).

89. Baddeley, A., Israel Exploits Space Technologies, Capabilities, Available online: https://www.afcea.org/content/israel-exploits-space-technologies-capabilities (accessed on 20 July 2020).

90. Curiel, A.D.S.; Whittaker, P.; Bird, R.; Haslehurst, A.; Nejadi, P.; Victoria, I.; Cawthorne, A.; Underwood, C.; Sweeting, M. Synthetic Aperture Radar on a Nanosatellite-is it Possible? In Proceedings of the 12th IAA Symposium on Small Satellites for Earth Observation. International Academy of Astronautics (IAA), Berlin, Germany, 6–10 May 2019.

91. Imbriale, W.A.; Gao, S.S.; Boccia, L. Space Antenna Handbook; John Wiley & Sons: Hoboken, NJ, USA, 2012.

92. Sharay, Y.; Naftaly, U. TECSAR: Design considerations and programme status. IEE Proc.-Radar Sonar Navig. 2006, 153, 117–121.

93. Jeong, S.Y.; Lee, S.Y.; Bae, M.J.; Cho, K.D. Configuration design of a deployable SAR antenna for space application and tool-kit development. Int. J. Aeronaut. Space 2014, 42, 683–691.

94. Wegner, P.M.; Ganley, J.; Maly, J.R. EELV secondary payload adapter (ESPA): Providing increased access to space. In Proceedings of the 2001 IEEE Aerospace Conference Proceedings

(Cat. No. 01TH8542), Big Sky, MT, USA, 10–17 March 2001; IEEE: 2011; Volume 5, pp. 2563–2568.

95. Caffrey, R. Using Rideshare to Launch CubeSats & ESPA S/C. In Proceedings of the 2nd Planetary CubeSat Science Symposium, Greenbelt, MD, USA, 26 September 2017.

96. Rosen, P.A.; Kumar, R. The NISAR Mission–An NASA/ISRO Space Partnership Supporting Global Research and Applications. In Proceedings of the 2019 URSI Asia-Pacific Radio Science Conference (AP-RASC), New Delhi, India, 9–15 March 2019; IEEE: 2019; pp. 1-1.

97. Freeman, A.; Johnson, W.T.K.; Huneycutt, B.; Jordan, R.; Hensley, S.; Siqueira, P.; Curlander, J. The" Myth" of the minimum SAR antenna area constraint. In Proceedings of the IEEE 1999 International Geoscience and Remote Sensing Symposium. IGARSS'99 (Cat. No. 99CH36293), Hamburg, Germany, 28 June–2 July 1999; IEEE, New York City, NY, USA: 1999; Volume 3, pp. 1770–1772.

98. Girard, R.; Plourde, P.; Séguin, G. The RADARSAT constellation payload design. In 2007 IEEE International Geoscience and Remote Sensing Symposium, Barcelona, Spain, 23–28 July 2007; IEEE, New York City, NY, USA: 2007; pp. 1387–1392.

99. de Almeida, F.Q.; Younis, M.; Krieger, G.; Moreira, A. An Analytical Error Model for Spaceborne SAR Multichannel Azimuth Reconstruction. IEEE Geosci. Remote S. 2017, 15, 853-857.

100. Akbar, P.R.; Sumantyo, J.T.S.; Saito, H. Design of synthetic aperture radar onboard small satellite. SANE. 2012, 112, 135–140.

101. Saito, H.; Pyne, B.; Tanaka, K.; Mita, M.; Kaneko, T.; Hirokawa, J., Tomura, T.; Watanabe, H.; Akbar, P.R.; Ijichi, K. Proto-Flight Model of SAR for 100kg class Small Satellite. In Proceedings of the 33rd Annual AIAA/USU Conference on Small Satellites, Logan, UT, USA. 3-8 August 2019.

102. Pyne, B.; Ravindra, V.; Saito, H. An improved pulse repetition frequency selection scheme for synthetic aperture radar. In Proceedings of the 2015 European Radar Conference (EuRAD), Paris, France, 9–11 September 2015; IEEE, New York City, NY, USA: 2015; pp. 257–260.

103. Pyne, B.; Akbar, P.; Saito, H.; Zhang, M.; Hirokawa, J.; Ando, M. Design of a center-feed waveguide feeder for wideband rectangular parallel-plate slot-array antenna on-board space-borne X-band SAR system. In Proceedings of the 2016 46th European Microwave Conference (EuMC), London, UK, 4–6 October 2016; IEEE, New York City, NY, USA: 2016; pp. 1533–1536.

104. Pyne, B.; Akbar, P.R.; Ravindra, V.; Saito, H.; Hirokawa, J.; Fukami, T. Slot-Array Antenna Feeder Network for Space-Borne X-Band Synthetic Aperture Radar. IEEE Trans. Antennas Propag. 2018, 66, 3463–3474.